



MoSe₂ nanosheets embedded in nitrogen/phosphorus co-doped carbon/graphene composite anodes for ultrafast sodium storage

Junxiong Wu ^a, Jiefu Yu ^a, Jiapeng Liu ^a, Jiang Cui ^a, Shanshan Yao ^a, Muhammad Ihsan-Ul Haq ^a, Nauman Mubarak ^a, Alessandro Susca ^a, Francesco Ciucci ^{a,b,c,*}, Jang-Kyo Kim ^{a,*}

^a Department of Mechanical and Aerospace Engineering, The Hong Kong University of Science and Technology, Clear Water Bay, Hong Kong, China

^b Department of Chemical and Biological Engineering, The Hong Kong University of Science and Technology, Clear Water Bay, Hong Kong, China

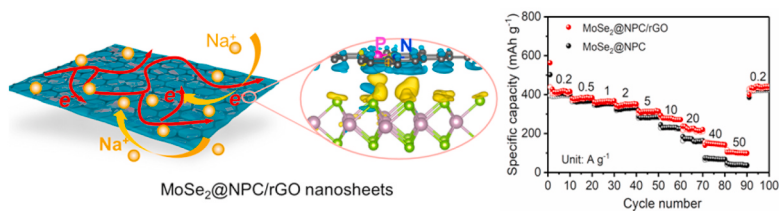
^c Guangzhou HKUST Fok Ying Tung Research Institute, Hong Kong, China



HIGHLIGHTS

- Few-layer MoSe₂ is embedded in an N/P co-doped carbon (NPC) matrix.
- The 2D feature of MoSe₂@NPC/rGO facilitates ultrafast Na storage.
- Theoretical calculations confirm the rapid mobility of Na on the surface of MoSe₂.
- MoSe₂@NPC/rGO nanosheets exhibit excellent rate capability even at 50 A g⁻¹.

GRAPHICAL ABSTRACT



ARTICLE INFO

Keywords:

MoSe₂
Carbon
Composite
Sodium-ion batteries
DFT calculations

ABSTRACT

Sodium-ion batteries have been considered a cost-effective alternative to lithium-ion batteries because of the cheap and abundant sodium reserves. However, the sluggish kinetics arising from the slow ion and electron transport, particularly at high rates, is the main bottleneck of fast sodium storage. Here, few-layer MoSe₂ encapsulated by nitrogen/phosphorus (N/P) co-doped carbon and reduced graphene oxide (MoSe₂@NPC/rGO) composites are fabricated through a simple polymerization reaction followed by selenization. The two-dimensional composite nanosheets effectively shorten the ion diffusion length while the few-layer MoSe₂ exposes a large surface area to the electrolyte. The NPC/rGO sheets intercalated within the composites function as channels for fast electron transfer and surface reactions. First-principles calculations show quick Na transport rates on the surface of MoSe₂, and quantitative kinetics analysis reveals a pseudocapacitance-dominated Na⁺ storage mechanism at high rates. Thanks to the ameliorating functional features and highly reversible conversion reactions, the MoSe₂@NPC/rGO electrode delivers a reversible capacity of ~340 mA h g⁻¹ after 500 cycles at 0.5 A g⁻¹ with a high contribution by surface capacitance. It also possesses a high reversible capacity of ~100 mA h g⁻¹ even at an extremely high current density of 50 A g⁻¹, presenting potential application as anodes for high-power sodium-ion batteries.

* Corresponding author. information: Department of Mechanical and Aerospace Engineering, The Hong Kong University of Science and Technology, Clear Water Bay, Hong Kong, China..

** Corresponding author. Department of Mechanical and Aerospace Engineering, The Hong Kong University of Science and Technology, Clear Water Bay, Hong Kong, China.

E-mail addresses: francesco.ciucci@ust.hk (F. Ciucci), mejkkim@ust.hk (J.-K. Kim).

1. Introduction

Due to the ever-increasing use of energy and the ensuing environmental pollution and global warming, the development of new energy storage devices with a long lifespan and low cost has triggered significant R&D efforts worldwide [1]. Lithium-ion batteries (LIBs) are currently the predominant devices powering portable electronics and electric vehicles [2–4]. However, the limited and uneven distribution of lithium (Li) resources and their high cost limit the application of LIBs in large-scale energy storage [5]. Considering the abundance of sodium (Na) in the earth's crust, sodium-ion batteries (SIBs) have been extensively explored as a promising alternative to LIBs [6,7]. However, Na is heavier than Li (23 vs. 6.9 g mol⁻¹) and has a higher redox potential (-2.71 and -3.04 V, respectively, versus standard hydrogen electrode). In addition, the larger ionic radius of Na results in a slower reaction kinetics and more significant volume expansion of active materials than Li ions [8–10]. As a result, SIBs suffer from poorer long-term cyclic stability with both lower energy and power densities than LIBs.

Although graphite is a well-developed anode for LIBs with a theoretical capacity of 372 mA h g⁻¹ [2], it failed to work in SIBs due to the unfavorable thermodynamics [6,11,12]. While a variety of carbon materials such as hard carbon [13], hollow carbon sphere [14], carbon fibers [15], have been explored as the potential anode materials, most of them presented low capacities (<250 mA h g⁻¹) with large initial capacity losses. Recently, considerable interest has been paid to the development of layer-structured transition metal dichalcogenides (TMDs) because of their large interlayer distances and high specific capacities [16]. For example, MoS₂, an extensively studied material for both LIBs and SIBs, has an interlayer distance of 6.2 Å and a high theoretical capacity of 670 mA h g⁻¹ [17–21]. MoSe₂ is analogous to MoS₂, having an even wider interlayer distance of 6.4 Å and a narrower bandgap of ~1.1 eV [22]. A larger spacing implies better diffusion, while a lower bandgap contributes to an improved electronic conductivity. Therefore, MoSe₂ is a promising material for fast Na storage. However, the electronic conductivity of MoSe₂ still needs further improvement for faster charging. Besides, the structural instability and agglomeration of MoSe₂ should be resolved to prevent rapid capacity decay.

Nanostructured MoSe₂/carbon (MoSe₂/C) composites were constructed to improve the electrochemical performance of MoSe₂, taking advantage of the ameliorating effect of carbon substrate [22–27]. To date, various MoSe₂/C hybrids, including MoSe₂@porous hollow carbon spheres [28], carbon-stabilized interlayer-expanded MoSe₂ nanosheets [24], fullerene-like MoSe₂ nanoparticles-embedded CNT balls [27], and MoSe₂ nanosheets vertically grown on graphene [22], have been reported. The size reduction of anode materials not only reduces the length of ion/electron transfer but also alleviates the strain arising from repetitive discharge/charge cycles. Meanwhile, carbon modification effectively enhances the electronic conductivity and structural integrity of composites during Na insertion/extraction. Nevertheless, these MoSe₂/C composites also have limitations because the MoSe₂ active material was either covered by amorphous carbon or directly grown on the surface of CNTs or graphene. If these nanocarbon materials act alone, it may be difficult to achieve both short-range electron transfer paths and long-range conductive networks. Moreover, the carbon matrices without heteroatoms, such as N-, P-, or S-doping, showed relatively low electronic conductivities and electrochemical reactivities [29,30]. This means that the design of anode materials requires proper modification of nanosized MoSe₂ to accelerate the mass transport and electron transfer rate.

With the aforementioned backdrop in mind, few-layer MoSe₂ nanosheets embedded in N/P co-doped carbon/graphene composites (MoSe₂@NPC/rGO) were prepared by *in-situ* polymerization and subsequent selenization. The MoSe₂@NPC/rGO composites had the following advantages: (i) the 2D structure had large surface reaction sites and short ion diffusion lengths; (ii) the graphene sheets intercalated

in the composites acted as both the channel for fast electron conduction and the substrate for rapid surface reactions; (iii) the few-layer MoSe₂ nanosheets are *in-situ* embedded in N/P co-doped porous carbon, preventing the agglomeration of MoSe₂ during electrochemical cycles and enhancing the structural stability of MoSe₂. The kinetics analysis revealed that the MoSe₂@NPC/rGO nanosheets had faster reaction kinetics than MoSe₂@NPC nanospheres. The first-principles calculations also confirmed the faster mobility of Na on the surface of MoSe₂ nanosheets than in the bulk counterparts and the ameliorating effect of N/P co-doped carbon matrix. As a result, the MoSe₂@NPC/rGO anode has shown excellent Na storage performance with high reversible capacities, ultrafast Na storage capability, and high cyclic stability.

2. Experimental section

2.1. Synthesis of MoSe₂@NPC/rGO, MoSe₂@NPC, and MoSe₂/rGO

The GO dispersion was prepared through the modified Hummers' method [31]. Specifically, 10 mL of GO suspension (1.0 mg mL⁻¹) was mixed with a phosphomolybdic acid solution (2.19 g phosphomolybdic acid (PMo₁₂) in 90 mL of deionized water) by ultrasonication. Then, a pyrrole (Py) solution (420 µL in 25 mL of ethanol) was slowly added into the mixture and stirred continuously for 12 h at RT. The precipitate (PPy-PMo₁₂/rGO) was collected and washed with ethanol several times and dried at 60 °C.

To obtain MoSe₂@NPC/rGO, PPy-PMo₁₂/rGO (100 mg) and Se powders were placed in porcelain boats at the downstream and upstream of a tube furnace. The furnace was heated to 650 °C and kept for 3 h under Ar(95%)/H₂(5%) flow, producing MoSe₂@NPC/rGO composites. For comparison, MoSe₂@NPC composites were also synthesized using the same method without GO during the polymerization.

The preparation of MoSe₂/rGO followed the previous study [25]. Specifically, 158 mg of Se was dissolved in 5 mL of N₂H₄·H₂O via vigorous stirring at 80 °C. Then, 10 mL of GO suspension (1.0 mg mL⁻¹) was mixed with Na₂MoO₄ solution (242 mg Na₂MoO₄·2H₂O in 20 mL deionized water). The Se-N₂H₄ solution was slowly added to the above solution and the resulting mixture was transferred to a 50-mL Teflon-lined autoclave and heated at 200 °C for 24 h. After cooling to RT, the black precipitate was separated by centrifugation and washed with deionized water and pure ethanol several times. The powders were dried at 60 °C in air and annealed at 650 °C for 3 h under Ar (95%)/H₂(5%) flow, and the final product was designated as MoSe₂/rGO.

2.2. Material characterizations

The XRD patterns were obtained using a Philips PW1830 diffractometer with Cu K α radiation at a scanning rate of 5° min⁻¹. The morphology and structure of synthesized materials were studied using field emission SEM (FE-SEM, JSM-7100, JEOL) and TEM (JEOL 2010F). The nitrogen adsorption/desorption isotherms, and the BET surface area were measured with a Micromeritics ASAP 2020 analyzer. The Raman spectra were collected using a Raman spectrometer (HORIBA Labram HR Evolution) equipped with a 532 nm Ar-ion laser. The XPS measurements were recorded using an ESCALAB 250Xi (Thermo Fisher) instrument with a monochromatic Al K α source. For the *ex-situ* XPS characterization, the MoSe₂@NPC/rGO anodes were rinsed with dimethyl carbonate (DMC) and dried in an Ar-filled glove box (Mbraun) before transferring to a vacuum chamber.

2.3. Electrochemical measurements

We prepared the electrodes by mixing the active materials (either MoSe₂@NPC/rGO or MoSe₂@NPC), carbon black, and sodium carboxymethyl cellulose at a weight ratio of 7:2:1 in deionized water to form a homogeneous slurry. The slurry was coated onto an aluminum foil and

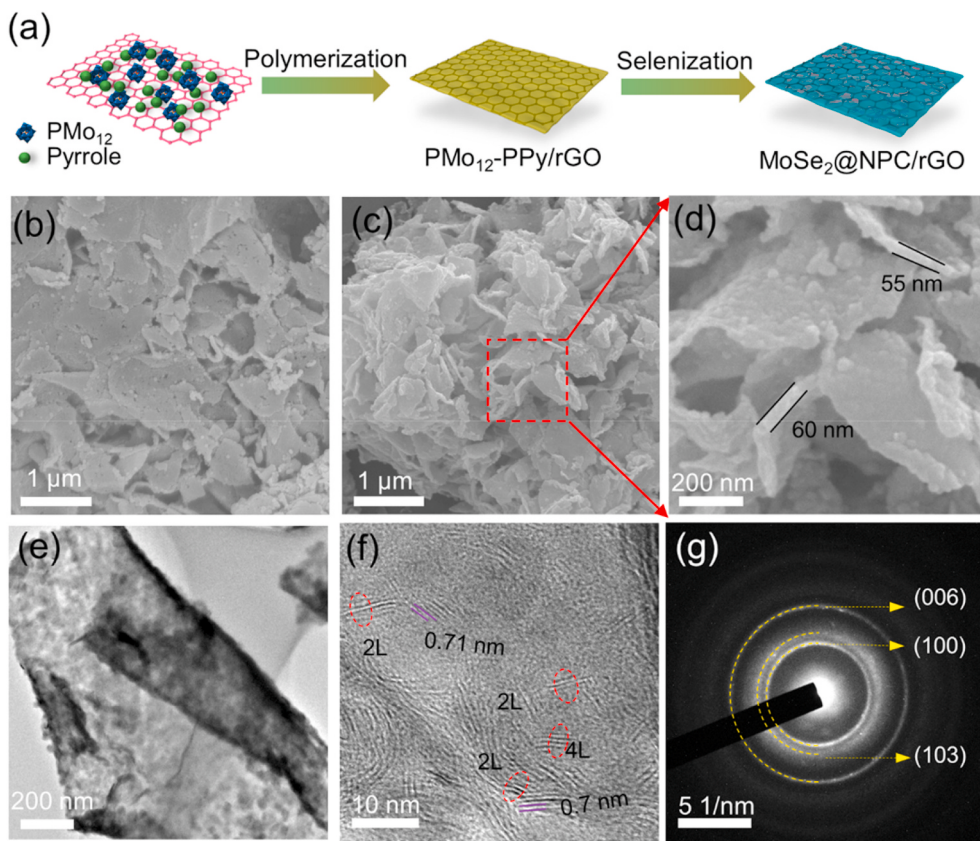


Fig. 1. (a) The preparation process of MoSe₂@NPC/rGO, (b) SEM image of PMo₁₂-PPy/rGO precursor, (c, d) SEM images, (e, f) TEM images, and (g) SAED pattern of MoSe₂@NPC/rGO.

dried in a vacuum oven at 100 °C for 12 h. Subsequently, the electrodes were punched into circular discs with a diameter of 12 mm and a loading of 1.0–1.2 mg cm⁻². The electrochemical performance of MoSe₂@NPC/rGO in SIBs was evaluated by assembling CR2032-type coin cells in an Ar-filled glove box with Na metal foil and glass microfiber (Whatman, GF/D) as the counter electrode and separator, respectively. 1 M NaClO₄ in propylene carbonate (PC) with 5 vol% fluoroethylene carbonate (FEC) was selected as the electrolyte. The electrochemical performance was measured on a battery testing system (Land 2001A) for a voltage range from 0.01 to 3 V at various current densities ranging from 0.2 to 50 A g⁻¹. CV measurements were performed using an electrochemical workstation (VSP-300, Biologic) between 0.01 and 3 V at a scan rate of 0.1 mV s⁻¹. EIS were carried out using the same workstation in the frequency range from 10 mHz to 100 kHz.

2.4. Computational methods

All spin-polarized DFT calculations were performed under the general gradient approximation (GGA) using the Perdew-Burke-Ernzerhof (PBE) functionals as implemented in the Vienna *ab initio* simulation package (VASP) [32,33]. The core-electrons were treated with the projector augmented wave method. The electrons in 2p⁶3s¹, 4p⁶5s¹4d⁵, 3s²3p⁴, 2s²2p², 2s²2p³, and 3s²3p³ states were treated as valence electrons for Na, Mo, S, C, N, and P, respectively. We also used the vdW-D3

functional to treat exchange and correlation, including a self-consistent van der Waals (vdW) correction [34]. The kinetic cutoff for plane-waves was set at 520 eV. For bulk calculations, a 3 × 3 × 1 supercell with the Mo₁₈Se₃₆ composition was used. For the surface calculations, a slab model with a 20 Å vacuum was employed to avoid self-interaction. The Brillouin zones of the bulk and surface calculations were sampled with 3 × 3 × 3 and 3 × 3 × 1 k-points, respectively. For each structural relaxation, both the ion positions and the lattice parameters were allowed to change until the Hellman-Feynman forces on each ion dropped below 0.02 eV Å⁻¹. The energy, E_{ad} , required to adsorb a Na atom on the surface or at the interlayer of MoSe₂ was calculated using:

$$E_{ad} = E_{\text{surface/bulk+Na}} - E_{\text{surface/bulk}} - E_{\text{Na}} \quad (1)$$

where $E_{\text{surface/bulk+Na}}$ is the total energy of an isolated Na atom either on the surface or at the interlayer of MoSe₂, $E_{\text{surface/bulk}}$ is the energy of MoSe₂ with the exposed (001) surface or the bulk MoSe₂, and E_{Na} is the energy of an isolated Na atom. The diffusion barrier of Na ions on the (001) surface or at the (001) interlayer was calculated using the CINEB method [35]. To predict the charge products, the formation energy, ΔE , of different oxidation products was estimated by DFT calculations using:

$$\Delta E = E_{\text{product}} - E_{\text{reactant}} \quad (2)$$

where E_{product} is the energy of MoSe₂ or Mo + Se, and E_{reactant} is the

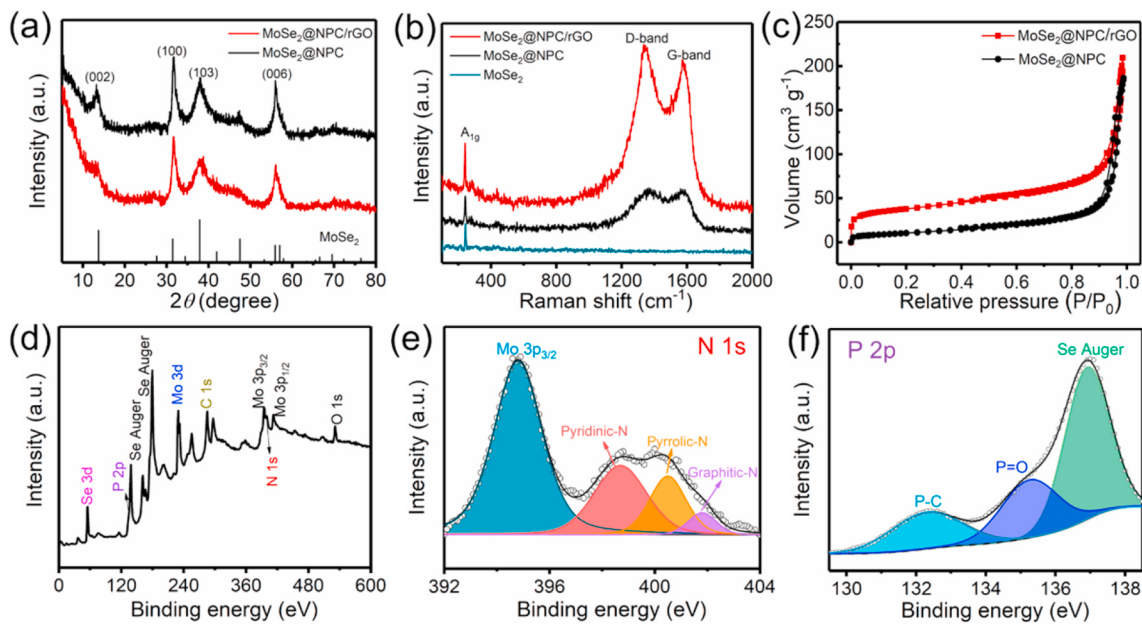


Fig. 2. (a) XRD patterns; (b) Raman spectra; and (c) N_2 adsorption/desorption isotherms of $MoSe_2@NPC$ and $MoSe_2@NPC/rGO$ composites; XPS spectra of $MoSe_2@NPC/rGO$: (d) survey scan, deconvoluted (e) N 1s, and (f) P 2p spectra.

energy of $Mo + Na_2Se$. We also performed the AIMD simulations at 600 K under the NVT ensemble with the Nosé thermostat to control the temperature [36,37]. The total simulation time was 30 ps with a time step of 1 fs? The MSD of Na was calculated using the following expression [37]:

$$MSD(\Delta t) = \frac{1}{N_{Na}} \sum_{i=1}^n |\mathbf{r}_i(t + \Delta t) - \mathbf{r}_i(t)|^2 \quad (3)$$

where N_{Na} is the total number of Na atoms in the MoS_2 supercell and \mathbf{r}_i is the trajectory of Na atoms.

3. Results and discussion

3.1. Characterization of $MoSe_2@NPC/rGO$

Fig. 1a schematically illustrates the synthesis process of $MoSe_2@NPC/rGO$ nanosheets. A Py solution was slowly added into a GO-phosphomolybdic acid dispersion under magnetic stirring. Then, the above mixture was stirred at room temperature (RT) for 20 h to obtain the PPy-PMo₁₂/rGO precursor. After gas selenization at 650 °C for 3 h, the $MoSe_2@NPC/rGO$ nanosheets were obtained. As shown in the scanning electron microscopy(SEM) image, the PPy-PMo₁₂/rGO precursor had a sheet-shaped structure, resulting from the polymerization of phosphomolybdic acid and Py on the surface of GO which functioned as 2D substrate (**Fig. 1b**). Upon simultaneous selenization and carbonization, the $MoSe_2@NPC/rGO$ presented a similar sheet structure with a thickness of ~55 nm, as shown in <https://www.nature.com/articles/ncomms11204> **Fig. 1c**. The energy-dispersive X-ray (EDX) spectrometer elemental maps exhibited uniformly distributed $MoSe_2$ on the N/P codoped carbon matrix (**Fig. S1**). The transmission electron microscopy (TEM) image shown in **Fig. 1e** verified the sheet structure of $MoSe_2@NPC/rGO$ composites. The $MoSe_2$ featured a few (<5) layers with a lattice spacing of ~0.7 nm corresponding to the (002) crystalline plane (**Fig. 1f**). The selected area electron diffraction (SAED) pattern presented in **Fig. 1g** indicates that $MoSe_2@NPC/rGO$ had a

polycrystalline structure. However, in the absence of GO sheets, the PPy-PMo₁₂ precursor and $MoSe_2@NPC$ featured a typical spherical structure with a uniform diameter of ~70 nm (see **Fig. S2**).

The X-ray diffraction (XRD) patterns of $MoSe_2@NPC/rGO$ and $MoSe_2@NPC$ are shown in **Fig. 2a**. Interestingly, the (002) characteristic peak at 13.7° is relatively weak in $MoSe_2@NPC/rGO$, indicating the existence of thin-layer $MoSe_2$. Another three peaks at 31.42°, 37.88°, and 55.92° can be indexed to the (100), (103), and (110) planes of the hexagonal $MoSe_2$ (JCPDS 29-0914). Both the Raman spectra of $MoSe_2@NPC/rGO$ and $MoSe_2@NPC$ in **Fig. 2b** displayed a distinct peak at 237.6 cm⁻¹, corresponding to the A_{1g} mode of $MoSe_2$ [25,38,39]. Another two peaks centered at ~1360 and 1591 cm⁻¹ are attributed to the D- and G-bands of carbon, respectively, exhibiting much stronger intensities in the former than the latter composites due to the presence of rGO in $MoSe_2@NPC/rGO$ [2,10]. The loadings of $MoSe_2$ in the two composites, as determined by the TGA analysis, were ~76 and 78 wt%, respectively, as shown in **Fig. S3**. The $MoSe_2@NPC/rGO$ nanosheets had a Brunauer-Emmett-Teller (BET) specific surface area of 133 m² g⁻¹, which is more than 3 times the $MoSe_2@NPC$ nanospheres (38 m² g⁻¹), see **Fig. 2c**. Notably, the specific surface area of $MoSe_2@NPC/rGO$ was larger than most reported $MoSe_2$ -based nanomaterials, such as $MoSe_2/G$ (52 m² g⁻¹) [22], $MoSe_2@CoSe/N$ -doped C (35.42 m² g⁻¹) [26], $MoSe_2/P-C@ TiO_2$ nanospheres (14.2 m² g⁻¹) [38], and $ZnSe/MoSe_2/C$ (70.1 m² g⁻¹) [40]. The large surface area is certainly advantageous because more sites are available for electrochemical reactions [41, 42].

The surface chemical state of $MoSe_2@NPC/rGO$ was investigated by X-ray photoelectron spectroscopy (XPS) analysis. The survey XPS spectrum (**Fig. 2d**) confirmed the presence of Mo, Se, C, N, and P elements. The deconvoluted Mo 3d spectrum (**Fig. S4a**) has peaks at 232.1 and 229.0 eV, corresponding to Mo^{4+} 3d_{3/2} and Mo^{4+} 3d_{5/2} in $MoSe_2$, respectively [25]. The Se 3d spectrum (**Fig. S4b**) presents two peaks located at 54.5 and 55.3 eV, attributed to Se 3d_{5/2} and Se 3d_{3/2}, respectively [26]. The C 1s spectrum (**Fig. S4c**) can be fitted by three peaks: the main peak at 284.8 eV corresponds to sp²-bonded C-C, and the two peaks at 285.2 and 286.5 eV relate to C-P/sp³-bonded C-C and

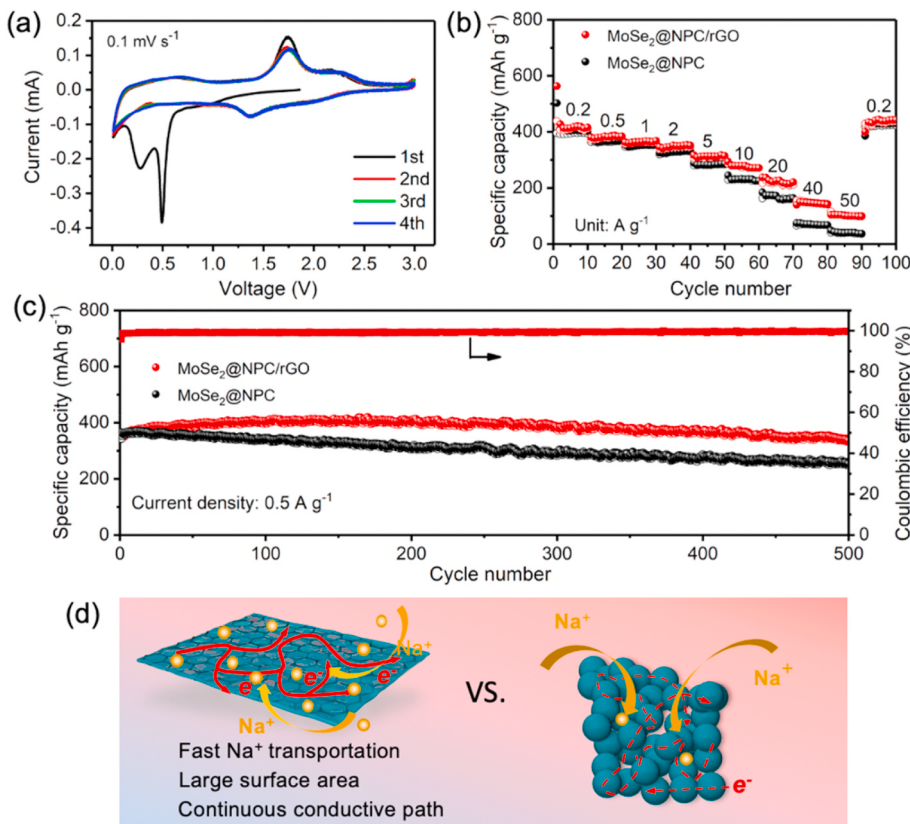
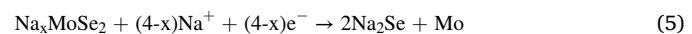
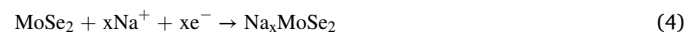


Fig. 3. (a) CV curves of MoSe₂@NPC/rGO half-cell scanned at 0.1 mV s⁻¹; (b) rate capabilities measured at current densities ranging from 0.2 to 50 A g⁻¹; (c) cyclic performance measured at 0.5 A g⁻¹; and (d) schematic illustrations of geometric features and electron/ion transport in the MoSe₂@NPC/rGO and MoSe₂@NPC electrodes.

C–N/C–O, respectively [43]. Moreover, the high-resolution spectra of N 1s and P 2p were also obtained where the N and P doping concentrations were measured to be ~3.4 and ~3.5 wt%, respectively. The N 1s XPS spectrum (Fig. 2e) indicates the existence of pyridinic-N (398.6 eV), pyrrolic-N (400.3 eV), and graphitic-N (401.2 eV) in the MoSe₂@NPC/rGO hybrid nanosheets [44]. The P 2p spectrum (Fig. 2f) displays two peaks at 132.6 and 135.4 eV, which are attributed to P–C and P=O bonds, respectively [45,46].

3.2. Electrochemical performance

Cyclic voltammetry (CV) measurements of the MoSe₂@NPC/rGO electrode were carried out between 0.01 and 3.0 V at a scan rate of 0.1 mV s⁻¹. As shown in Fig. 3a, the first cathodic scan had two sharp peaks at 0.5 and 0.25 V. The reduction peak at 0.5 V can be attributed to the intercalation of Na⁺ into the lattice of MoSe₂ to form Na_xMoSe₂ [47]. The other peak at 0.25 V can be correlated with the conversion reaction from Na_xMoSe₂ to Mo metal and Na₂Se along with the formation of a solid electrolyte interphase (SEI) layer [48]. These two reactions can be described by:



The sharp peak observed at 1.7 V in the following anodic scan corresponds to the oxidation of Mo [23,24]. From the second cycle and onwards, the reduction and oxidation scans nearly overlapped, indicating high reversibility of the reactions taking place in the MoSe₂@NPC/rGO electrode. Fig. S5 shows the galvanostatic charge/discharge (GCD) profiles for the initial three cycles obtained at a current density of 0.2 A g⁻¹. The initial discharge and charge capacities of the MoSe₂@NPC/rGO electrode were 563.2 and 438.5 mA h g⁻¹, corresponding to an initial Coulombic efficiency (CE) of 78%. The capacity loss during the first cycle was mainly due to the formation of SEI film [10]. The rate capability of the MoSe₂@NPC/rGO electrode is displayed in Fig. 3b. As the current density was increased from 0.2 to 0.5, 1, 2, 5, 10, 20, 40, and 50 A g⁻¹, its reversible capacity gradually decreased from ~415 to 380, 360, 350, 310, 280, 220, 150, and 100 mA h g⁻¹, respectively. In comparison, the reversible capacities of the MoSe₂@NPC electrode were much lower, namely ~70 and 35 mA h g⁻¹ at 40 and 50 A g⁻¹, respectively. The cyclic performance of both electrodes was measured at 0.5 A g⁻¹, see Fig. 3c. The MoSe₂@NPC/rGO

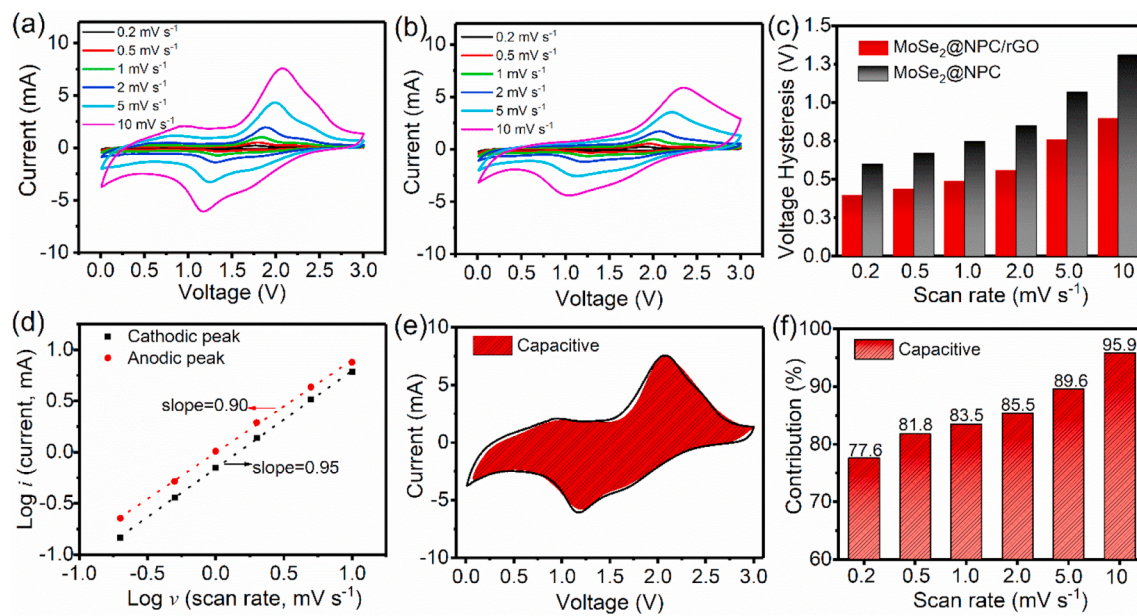


Fig. 4. CV curves of (a) the MoSe₂@NPC/rGO and (b) MoSe₂@NPC electrodes at different scan rates ranging from 0.2 to 10 mV s⁻¹. (c) Summary of voltage hysteresis of MoSe₂@ NPC/rGO and MoSe₂@NPC; and the corresponding (d) log (*i*) versus log (*v*) plots at cathodic and anodic peaks. (e) Capacitive contribution (red area) of MoSe₂@NPC/rGO at 10 mV s⁻¹; and (f) the percentage of capacitive contributions at scan rates ranging from 0.2 to 10 mV s⁻¹. (For interpretation of the references to colour in this figure legend, the reader is referred to the Web version of this article.)

electrode delivered a reversible capacity of 340 mA h g⁻¹ with 94% retention after 500 cycles, whereas the MoSe₂@NPC counterpart exhibited 75% capacity retention after 500 cycles. Also, the electrochemical performance of MoSe₂/rGO was also examined to compare with MoSe₂@NPC/rGO. As shown in Fig. S6, the cyclic stability and rate capability of MoSe₂/rGO were much worse than MoSe₂@NPC/rGO, implying the positive effect of N/P co-doping of carbon matrix via enhanced electron transfer. Therefore, the much better rate capabilities and cyclic stability of the MoSe₂@NPC/rGO electrode can be attributed to the interconnected electron conduction paths through the NPC and rGO components, abundant active sites for Na⁺ storage, and fast transport of Na⁺, and these ameliorating features are schematically illustrated in Fig. 3d. The comparison of rate capabilities of the current MoSe₂@NPC/rGO electrode with state-of-the-art results reported for similar MoSe₂-based electrodes in SIBs (Fig. S7) indicates that the capacities of the MoSe₂@NPC/rGO electrode were among the best, particularly at high current densities of 10 A g⁻¹ and beyond.

3.3. Kinetic analysis

Further, CV measurements were conducted to study the reaction kinetics. The MoSe₂@NPC/rGO electrode had much smaller peak shifts in both cathodic and anodic scans than the MoSe₂@NPC electrode, as shown in Fig. 4a and b, indicating less polarization in the former electrode. Fig. 4c displays the voltage hysteresis when the scan rate was increased from 0.2 to 10 mV s⁻¹, which measures the voltage difference between cathodic and anodic peaks. The hysteresis in the MoSe₂@NPC/rGO electrode increased from 0.35 to 0.85 V, whereas the corresponding values were 0.6 and 1.4 V for MoSe₂@NPC. Therefore, it can be said that MoSe₂@NPC/rGO has faster reaction kinetics than MoSe₂@NPC. The charge storage behavior was analyzed according to the power-law relationship [49]:

$$i = av^b \quad (6)$$

where *i* is the peak current (mA), *v* is the scan rate (mV s⁻¹), and *a* and *b* are the adjustable parameters. The *b* value can be obtained by fitting the line, log (*i*) versus log (*v*). There are two well-defined conditions: (i) *b* = 0.5 indicates a diffusion-controlled charge storage mechanism indicative of a battery reaction process; (ii) *b* = 1 implies a capacitive process. The *b* values were 0.95 and 0.90, respectively, for the cathodic and anodic peaks of the MoSe₂@NPC/rGO electrode, as shown in Fig. 4d. In contrast, the corresponding *b* values of the MoSe₂@NPC counterpart were 0.87 and 0.82, much lower than those of the former electrode (Fig. S8), signifying a higher and pseudocapacitance-dominated contribution in the MoSe₂@NPC/rGO electrode. Specifically, the pseudocapacitive contribution to the current response can be quantitatively separated based on Equation (7) [50]:

$$i(V) = k_1(V) \cdot v + k_2(V) \cdot v^{1/2} \quad (7)$$

where *k*₁ and *k*₂ are the functions of potential, and *k*₁(V) · *v* and *k*₂(V) · *v*^{1/2} correspond to the pseudocapacitance- and the diffusion-controlled contributions, respectively. Approximately 96% of total capacity was attributed to capacitance at a scan rate of 10 mV s⁻¹, as shown in Fig. 4e, while Fig. 4f shows the pseudocapacitive contributions at different scan rates. It is seen that the capacitive component increased from ~78% to ~96% with increasing scan rate from 0.2 to 10 mV s⁻¹, similar to recent reports on Mo₂S/C [10] and Sn₂S/graphene-CNT aerogel anodes [51]. This implies that the superior high-rate performance can be ascribed to the pseudocapacitance originating from the 2D architecture with the enhanced specific surface area.

The improved Na⁺ reaction kinetics of the MoSe₂@ NPC /rGO electrode is further supported by the smaller charge transfer resistance (*R*_{ct}) than that of the MoSe₂@ NPC electrode. The electrochemical impedance spectra (EIS) reported in Fig. S9a were fitted by the equivalent circuit (inset of Fig. S9a). The *R*_{ct} values of the MoSe₂@NPC/rGO and MoSe₂@NPC electrodes were 51.9 and 109.2 Ω (Table S1), respectively, signifying faster electrochemical kinetics of the former

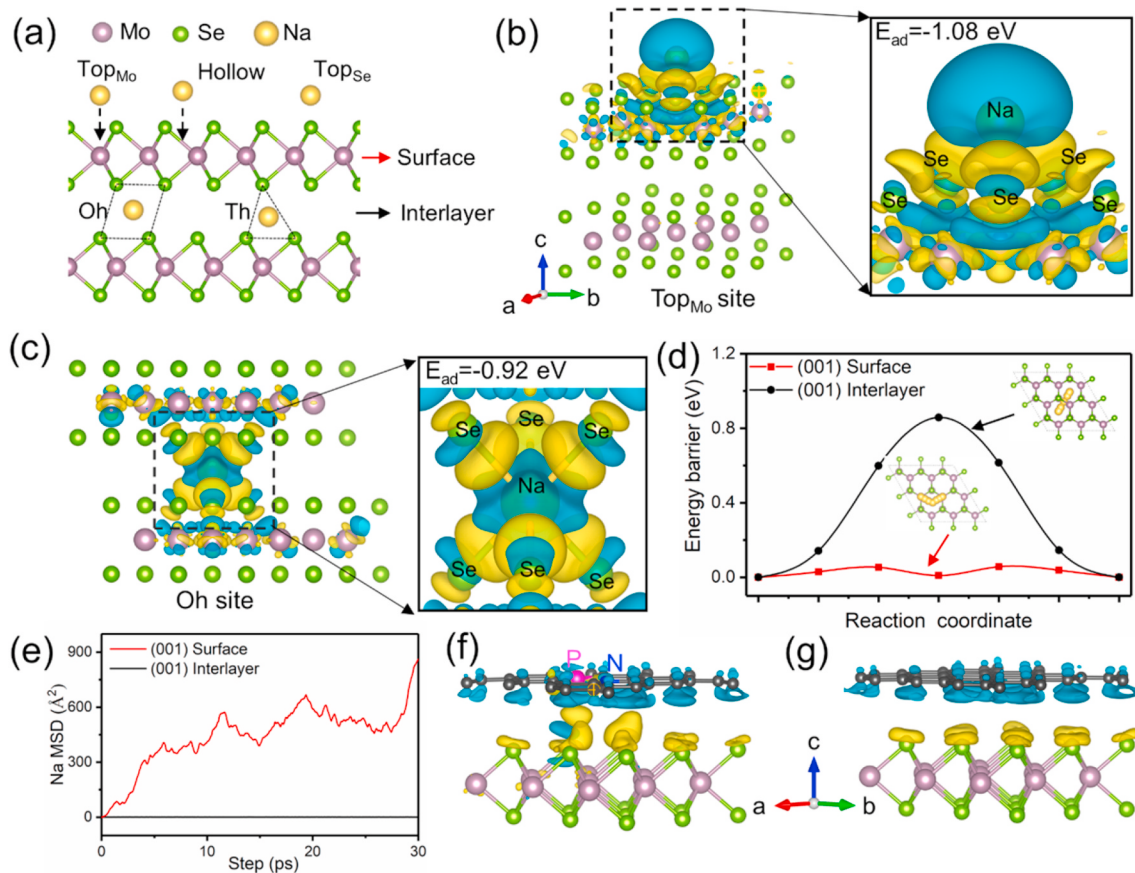


Fig. 5. (a) Schematic illustration of Na adsorption sites on the (001) surface and in the (001) interlayer; Charge density difference plots of an isolated Na on the (001) surface (b) and at the (001) interlayer (c). (d) Na diffusion energy profiles on the (001) surface and at the (001) interlayer. The inset pictures show the corresponding Na diffusion paths; and (e) Na MSD in (001) interlayer and on (001) surface. Charge density difference plots of relaxed MoSe₂ on (f) N/P co-doped carbon (NPC) and (g) pure C.

electrode than the latter. The Z' vs. $\omega^{-1/2}$ ($\omega = 2\pi f$) curves in the low-frequency region are shown in Fig. S9b. The Na^+ diffusion coefficient (D_{Na}^+) of the MoSe₂@NPC/rGO electrode was twice higher than the MoSe₂@NPC (see the details in SI), consistent with the voltage hysteresis (Fig. 4c) and R_{ct} values (Table S1).

3.4. First-principles calculations

According to previous studies, downsizing the active materials has a positive impact on the electrochemical performance of the electrodes due to the improved ionic diffusion, surface areas, and fracture toughness [52,53]. We combined the density functional theory (DFT) and *ab initio* molecular dynamics (AIMD) calculations to study the Na adsorption and diffusion on the (001) surface and along the interlayer of MoSe₂. The adsorption energies of an isolated Na atom in the two models were calculated according to Equation (1). The structure corresponding to an isolated Na atom adsorbed on the surface or intercalated is shown in Fig. 5a and the adsorption energies are reported in Table S2. The results confirm that the surface sites preferably host Na atoms, giving rise to a higher adsorption capacitance. Fig. 5b and c shows the charge density differences of an isolated Na adsorbed at the Top_{Mo} site on the surface and the Oh site in the interlayer, respectively. The

adsorption energies obtained for the two configurations were -1.22 (Top_{Mo} site) and -0.92 eV (Oh site), respectively, indicating a stronger Na adsorption on the surface of MoSe₂ than that in the interlayer. The charge density difference in Na adsorption process was calculated by $\Delta\rho = \rho(\text{MoSe}_2+\text{Na})-\rho(\text{MoSe}_2)-\rho(\text{Na})$, where $\rho(\text{MoSe}_2+\text{Na})$, $\rho(\text{MoSe}_2)$, and $\rho(\text{Na})$ are the total charges of the system, MoSe₂, and Na atom, respectively. The yellow and cyan surfaces correspond to the charge gain and loss regions, respectively.

We also used the climbing image nudged elastic band (CINEB) method to estimate the Na diffusional barriers for the two configurations, and the results are given in Fig. 5d. The energy barrier, 56.5 meV, for Na hopping on the (001) surface was much smaller than that along the (001) interlayer, indicating a much higher Na mobility on the surface. These findings were compared quantitatively with those obtained by AIMD simulations. The mean-squared displacement (MSD) values obtained by AIMD simulations are shown in Fig. 5e. The diffusion coefficients D_{Na}^+ on the MoSe₂ surface and at the interlayer determined at 600 K were 2.56×10^{-4} and $1.94 \times 10^{-9} \text{ cm}^2 \text{ s}^{-1}$, respectively. In agreement with the CINEB results, the mobility of Na atoms on the surface was consistently higher than that in the interlayer.

To verify the ameliorating effect of N/P co-doping of carbon matrix, the electronic interactions of MoSe₂ with NPC and pure C were

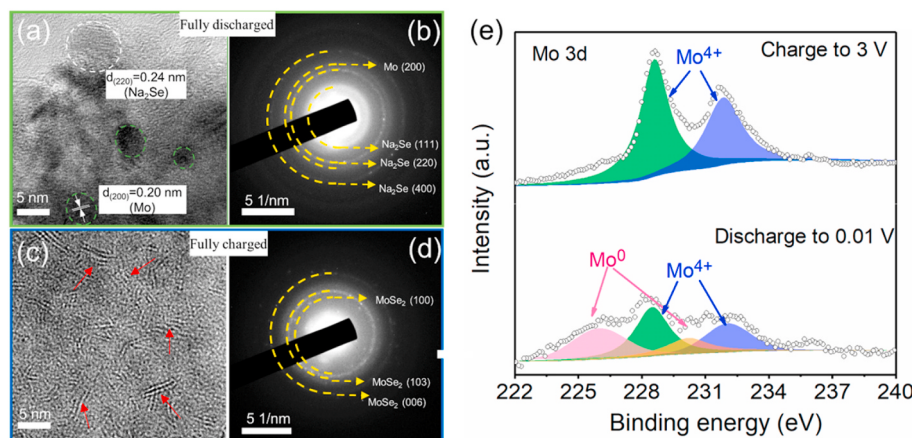


Fig. 6. *Ex-situ* high-resolution TEM images and corresponding SAED patterns of the cycled MoSe₂@PC/rGO electrode (a, b) at a fully sodiated state and (c, d) at a fully desodiated state. (e) *Ex-situ* high-resolution Mo 3d XPS spectra of MoSe₂@NP/rGO at fully charged and discharged states.

compared. N/P co-doped and pristine graphene sheets were used to model the NPC and pure C, as shown in Fig. 5f and g, respectively. There was significant electron transfer from NPC to MoSe₂, whereas the interaction between MoSe₂ and pure C was relatively weak. Na₂Se is the discharge product of MoSe₂ formed after a conversion reaction, see Equation (5). Therefore, the adsorption of Na₂Se on carbon matrix is essential because it would affect the uniform distribution of discharge products. As shown in Fig. S10, the adsorption energies of Na₂Se on NPC, and pure C were evaluated. The NPC substrate presented a much higher Na₂Se adsorption energy of -1.51 eV than -0.79 eV of pure C, corroborating better adsorption and reversible reaction of Na₂Se on the former than the latter surface. To confirm its stability, we analyzed the MoSe₂@NPC/rGO composite SEM and TEM characterizations after 100 charge and discharge cycles at 0.5 A g⁻¹. Thanks to the strong coupling between the NPC substrate and MoSe₂, the material structure and nanosheet morphology are preserved (Figs. S11a and b). Also, the EDS elemental maps of the cycled MoSe₂@NPC/rGO electrode (Fig. S11c) suggest that each element is homogeneously distributed through the samples, further demonstrating the excellent structural stability.

3.5. Sodium storage mechanism

To analyze the reaction mechanism between Na⁺ and MoSe₂, *ex-situ* XPS and TEM were performed to elucidate the phase change of MoSe₂ during the sodiation/desodiation process. We tried to identify the discharge and recharge products of MoSe₂@NPC/rGO composites with XRD but failed to find any viable information, probably due to the poor crystallinity of the products. Therefore, *ex-situ* TEM analysis was used to investigate the charge and discharge products. As shown in Fig. 6a, the lattice spacings indexed to Mo (200) and Na₂Se indicate that a complete conversion reaction occurred when the composite was discharged to 0.01 V. The SAED pattern confirmed the diffraction rings of both Mo (200) and Na₂Se (111) (Fig. 6b), in agreement with the literature. After full recharging to 3.0 V, the few-layer MoSe₂ nanosheets were identified from the high-resolution TEM image (Fig. 6c), which are verified by the diffraction rings in the SAED pattern (Fig. 6d). *Ex-situ* deconvoluted Mo XPS spectra of MoSe₂@NP/rGO at fully charged and discharged states are shown in Fig. 6e. Upon discharging to 0.01 V, the peaks located at 228.2 and 232 eV are assigned to Mo⁴⁺. The peaks at 226 and 230.5 eV correspond to elemental Mo⁰, indicating the reduction of MoSe₂ to Mo

metal during discharge [54]. When the battery was recharged to 3 V, only the peaks of Mo⁴⁺ were observed, confirming the reversibility of conversion reactions. The Se 3d spectrum at a charged state is shown in Fig. S12, exhibiting two peaks at 54.1 and 55.1 eV, which are assigned to Se²⁻ instead of elemental Se [55]. It is noticed that after recharging to 3 V both the Mo 3d and Se 3d peaks down-shifted by about 0.3 eV, a reflection of the change in electron environment caused by donation of electrons from Na to MoSe₂ [56–58], confirming again the reversible conversion reaction of MoSe₂@NPC/rGO during the sodiation and desodiation cycles. Furthermore, the DFT calculations were applied to estimate the formation energies of two possible reactions, as shown in Table S3. The formation energy of MoSe₂ was lower than that of Se, *i.e.*, 3.51 vs. 6.42 eV, indicating the charge product being more likely to be MoSe₂ than Se. This result also agrees with the experiments. Given the consistent results of TEM, XPS, and DFT calculations, the reversible conversion reaction of MoSe₂ during discharge and charge is verified (Fig. S13).

4. Conclusions

In conclusion, we synthesized the MoSe₂@NPC/rGO nanosheet composites by a novel and simple two-step strategy, namely *in-situ* polymerization and high-temperature gas selenization. The 2D structure of MoSe₂@NPC/rGO composites facilitated reduced ion diffusion lengths, and the few-layer MoSe₂ exposed a large surface area for fast Na⁺ transportation. The NPC/rGO substrate improved the electrical conductivity and structural stability with a low charge transfer resistance, giving rise to enhanced Na storage kinetics. The *ex-situ* TEM, *ex-situ* XPS, and DFT calculations verified highly reversible conversion reactions of MoSe₂ nanosheets during the sodiation/desodiation cycles of the composite electrode. Benefiting from these ameliorating functional and structural features as well as high reversible conversion reactions, the MoSe₂@NPC/rGO electrode delivered high reversible capacities, long cyclic stability, and an excellent rate capability in SIBs.

CRediT authorship contribution statement

Junxiong Wu: Conceptualization, Methodology, Formal analysis, Investigation, Writing - original draft. **Jiefu Yu:** Methodology, Formal analysis, Investigation. **Jiapeng Liu:** Software. **Jiang Cui:**

Methodology, Formal analysis, Investigation. **Shanshan Yao:** Methodology, Formal analysis, Investigation. **Muhammad Ihsan-Ul Haq:** Formal analysis. **Nauman Mubarak:** Formal analysis. **Alessandro Susca:** Formal analysis. **Francesco Ciucci:** Resources, Funding acquisition, Writing - review & editing, Supervision. **Jang-Kyo Kim:** Resources, Funding acquisition, Writing - review & editing, Supervision.

Declaration of competing interest

The authors declare that they have no known competing financial interests or personal relationships that could have appeared to influence the work reported in this paper.

Acknowledgments

This project was financially supported by the Research Grants Council (GRFProjects: 16207615, 16227016, 16204517, and 16208718) and the Innovation and Technology Commission (ITFproject ITS/001/17 and ITS/292/18FP) of Hong Kong SAR. The authors also acknowledge the support from the Guangzhou Science and Technology Program (No. 201807010074). The authors also appreciate the technical assistance from the Advanced Engineering Materials facilities (AEMF) and the Materials Characterization and Preparation Facilities (MCPF) of HKUST.

Appendix A. Supplementary data

Supplementary data to this article can be found online at <https://doi.org/10.1016/j.jpowsour.2020.228660>.

References

- [1] J.-M. Tarascon, M. Armand, *Nature* 414 (2001) 359–367.
- [2] J. Wu, X. Qin, H. Zhang, Y.-B. He, B. Li, L. Ke, W. Lv, H. Du, Q.-H. Yang, F. Kang, *Carbon* 84 (2015) 434–443.
- [3] J. Wu, X. Qin, C. Miao, Y.-B. He, G. Liang, D. Zhou, M. Liu, C. Han, B. Li, F. Kang, *Carbon* 98 (2016) 582–591.
- [4] S.W. Kim, D.H. Seo, X. Ma, G. Ceder, K. Kang, *Adv. Energy Mater.* 2 (2012) 710–721.
- [5] H. Zhou, *Energy Environ. Sci.* 6 (2013), 2256–2256.
- [6] J. Cui, S. Yao, J.-K. Kim, *Energy Storage Mater.* 7 (2017) 64–114.
- [7] N. Yabuuchi, K. Kubota, M. Dahbi, S. Komaba, *Chem. Rev.* 114 (2014) 11636–11682.
- [8] S. Yao, J. Cui, Z. Lu, Z.L. Xu, L. Qin, J. Huang, Z. Sadighi, F. Ciucci, J.-K. Kim, *Adv. Energy Mater.* 7 (2017) 1602149.
- [9] J. Cui, Z.-L. Xu, S. Yao, J. Huang, J.-Q. Huang, S. Abouali, M.A. Garakani, X. Ning, J.-K. Kim, *J. Mater. Chem.* 4 (2016) 10964–10973.
- [10] J. Wu, Z. Lu, K. Li, J. Cui, S. Yao, M. Ihsan-Ul-Haq, B. Li, Q.-H. Yang, F. Kang, F. Ciucci, J.-K. Kim, *J. Mater. Chem.* 6 (2018) 5668–5677.
- [11] S. Yao, J. Cui, J. Huang, J.Q. Huang, W.G. Chong, L. Qin, Y.W. Mai, J.-K. Kim, *Adv. Energy Mater.* 8 (2018) 1702267.
- [12] J. Qian, Y. Xiong, Y. Cao, X. Ai, H. Yang, *Nano Lett.* 14 (2014) 1865–1869.
- [13] B. Zhang, C.M. Ghimbeu, C. Laberty, C. Vix-Guterl, J.-M. Tarascon, *Adv. Energy Mater.* 6 (2016) 1501588.
- [14] K. Tang, L. Fu, R.J. White, L. Yu, M.M. Titirici, M. Antonietti, J. Maier, *Adv. Energy Mater.* 2 (2012) 873–877.
- [15] S. Wang, L. Xia, L. Yu, L. Zhang, H. Wang, X.W. Lou, *Adv. Energy Mater.* 6 (2016) 1502217.
- [16] W. Ding, L. Hu, J. Dai, X. Tang, R. Wei, Z. Sheng, C. Liang, D. Shao, W. Song, Q. Liu, M. Chen, X. Zhu, S. Chou, X. Zhu, Q. Chen, Y. Sun, S. Dou, *ACS Nano* 13 (2019) 1694–1702.
- [17] T. Wang, S. Chen, H. Pang, H. Xue, Y. Yu, *Adv. Sci.* 4 (2017) 1600289.
- [18] Z. Hu, Q. Liu, S.L. Chou, S.X. Dou, *Adv. Mater.* 29 (2017) 1700606.
- [19] D. Sun, D. Huang, H. Wang, G.-L. Xu, X. Zhang, R. Zhang, Y. Tang, D.A. El-Hady, W. Alshitar, A.S. Al-Bogami, K. Amine, M. Shao, *Nano Energy* 61 (2019) 361–369.
- [20] J. Wu, F. Ciucci, J.-K. Kim, *Chem. Eur. J.* 26 (2020) 1–26.
- [21] J. Wu, J. Liu, J. Cui, S. Yao, M. Ihsan-Ul-Haq, N. Mubarak, E. Quattrochi, F. Ciucci, J.-K. Kim, *J. Mater. Chem.* 8 (2020) 2114–2122.
- [22] X. Zhao, W. Cai, Y. Yang, X. Song, Z. Neale, H.-E. Wang, J. Sui, G. Cao, *Nano Energy* 47 (2018) 224–234.
- [23] F. Zheng, W. Zhong, Q. Deng, Q. Pan, X. Ou, Y. Liu, X. Xiong, C. Yang, Y. Chen, M. Liu, *Chem. Eng. J.* 357 (2019) 226–236.
- [24] Y. Tang, Z. Zhao, Y. Wang, Y. Dong, Y. Liu, X. Wang, J. Qiu, *ACS Appl. Mater. Interfaces* 8 (2016) 32324–32332.
- [25] F. Niu, J. Yang, N. Wang, D. Zhang, W. Fan, J. Yang, Y. Qian, *Adv. Funct. Mater.* 27 (2017) 1700522.
- [26] J. Chen, A. Pan, Y. Wang, X. Cao, W. Zhang, X. Kong, Q. Su, J. Lin, G. Cao, S. Liang, *Energy Storage Mater.* 21 (2019) 97–106.
- [27] S.H. Choi, Y.C. Kang, *Nanoscale* 8 (2016) 4209–4216.
- [28] X. Yang, Z. Zhang, Y. Fu, Q. Li, *Nanoscale* 7 (2015) 10198–10203.
- [29] L. Fu, K. Tang, K. Song, P.A. van Aken, Y. Yu, J. Maier, *Nanoscale* 6 (2014) 1384–1389.
- [30] J.P. Paraknowitsch, A. Thomas, *Energy Environ. Sci.* 6 (2013) 2839–2855.
- [31] J. Jia, C.-M. Kan, X. Lin, X. Shen, J.-K. Kim, *Carbon* 77 (2014) 244–254.
- [32] G. Kresse, J. Furthmüller, *Phys. Rev. B* 54 (1996) 11169–11186.
- [33] J.P. Perdew, K. Burke, M. Ernzerhof, *Phys. Rev. Lett.* 77 (1996) 3865–3868.
- [34] S. Grimme, J. Antony, S. Ehrlich, H. Krieg, *J. Chem. Phys.* 132 (2010) 154104.
- [35] G. Henkelman, B.P. Uberuaga, H. Jónsson, *J. Chem. Phys.* 113 (2000) 9901.
- [36] J. Wu, J. Liu, Z. Lu, K. Lin, Y.-Q. Lyu, B. Li, F. Ciucci, J.-K. Kim, *Energy Storage Mater.* 23 (2019) 8–16.
- [37] J. Liu, Z. Lu, M.B. Effat, F. Ciucci, *J. Power Sources* 409 (2019) 94–101.
- [38] Y. Wang, Y. Wang, W. Kang, D. Cao, C. Li, D. Cao, Z. Kang, D. Sun, R. Wang, Y. Cao, *Adv. Sci.* 6 (2019) 1801222.
- [39] J. Kang, Q. Su, H. Feng, P. Huang, G. Du, B. Xu, *Electrochim. Acta* 301 (2019) 29–38.
- [40] L. Zeng, Y. Fang, L. Xu, C. Zheng, M. Yang, J. He, H. Xue, Q. Chen, M. Wei, Q. Qian, *Nanoscale* 11 (2019) 6766–6775.
- [41] W. Ren, H. Zhang, C. Guan, C. Cheng, *Adv. Funct. Mater.* 27 (2017) 1702116.
- [42] J.B. Cook, H.-S. Kim, Y. Yan, J.S. Ko, S. Robbennolt, B. Dunn, S.H. Tolbert, *Adv. Energy Mater.* 6 (2016) 1501937.
- [43] Z. Lin, G. Waller, Y. Liu, M. Liu, C.P. Wong, *Adv. Energy Mater.* 2 (2012) 884–888.
- [44] Z. Liu, H. Nie, Z. Yang, J. Zhang, Z. Jin, Y. Lu, Z. Xiao, S. Huang, *Nanoscale* 5 (2013) 3283–3288.
- [45] M.A. Patel, F. Luo, M.R. Khoshi, E. Rabie, Q. Zhang, C.R. Flach, R. Mendelsohn, E. Garfunkel, M. Szostak, H. He, *ACS Nano* 10 (2016) 2305–2315.
- [46] Y.-Y. Chen, Y. Zhang, W.-J. Jiang, X. Zhang, Z. Dai, L.-J. Wan, J.-S. Hu, *ACS Nano* 10 (2016) 8851–8860.
- [47] Y.N. Ko, S. Choi, S. Park, Y.C. Kang, *Nanoscale* 6 (2014) 10511–10515.
- [48] H. Liu, B. Liu, H. Guo, M. Liang, Y. Zhang, T. Borjigin, X. Yang, L. Wang, X. Sun, *Nano Energy* 51 (2018) 639–648.
- [49] Z. Hu, L. Wang, K. Zhang, J. Wang, F. Cheng, Z. Tao, J. Chen, *Angew. Chem. Int. Ed.* 53 (2014) 12794–12798.
- [50] H.-S. Kim, J.B. Cook, H. Lin, J.S. Ko, S.H. Tolbert, V. Ozolins, B. Dunn, *Nat. Mater.* 16 (2017) 454–460.
- [51] J. Cui, S. Yao, Z. Lu, J.Q. Huang, W.G. Chong, F. Ciucci, J.-K. Kim, *Adv. Energy Mater.* 8 (2018) 1702488.
- [52] Z.-L. Xu, X.M. Liu, Y.S. Luo, L.M. Zhou, J.-K. Kim, *Prog. Mater. Sci.* 90 (2017) 1–44.
- [53] S.-K. Jung, I. Hwang, D. Chang, K.-Y. Park, S.J. Kim, W.M. Seong, D. Eum, J. Park, B. Kim, J. Kim, J.H. Heo, K. Kang, *Chem. Rev.* (2019), <https://doi.org/10.1021/acs.chemrev.9b00405>.
- [54] S. Hao, X. Shen, M. Tian, R. Yu, Z. Wang, L. Chen, *Nano Energy* 41 (2017) 217–224.
- [55] S. Xin, L. Yu, Y. You, H.-P. Cong, Y.-X. Yin, X.-L. Du, Y.-G. Guo, S.-H. Yu, Y. Cui, J. B. Goodenough, *Nano Lett.* 16 (2016) 4560–4568.
- [56] N.P. Kondekar, M.G. Boebinger, E.V. Woods, M.T. McDowell, *ACS Appl. Mater. Interfaces* 9 (2017) 32394–32404.
- [57] H. Wu, Y. Wu, X. Chen, Y. Ma, M. Xu, W. Wei, J. Pan, X. Xiong, *RSC Adv.* 6 (2016) 23161–23168.
- [58] H. Wang, Z. Lu, S. Xu, D. Kong, J.J. Cha, G. Zheng, P.-C. Hsu, K. Yan, D. Bradshaw, F.B. Prinz, *Proc. Natl. Acad. Sci.* 110 (2013) 19701–19706.